Unsteady simulations of an aircraft with installed engine and rotating fan

Fulvio Sartor

DOI: 10.13009/EUCASS2023-597
Aerospace Europe Conference 2023 – 10TH EUCASS – 9TH CEAS

Unsteady simulations of an aircraft with installed engine and rotating fan

Fulvio Sartor
ONERA, DAAA/ACI, 8 rue des Vertugadins, 92190 Meudon, France
fulvio.sartor@onera.fr

Abstract

Numerical simulations have been performed to reproduce the flow around an aircraft with installed engine and rotating fan, by modelling the external aerodynamics of the plane as well as the internal aerodynamics in the secondary flow of the engine, located under the wing. These calculations take into account most of the elements of a civil transport aircraft and allow to finely model the interactions between the engine and the airframe. The analysis allows for an evaluation of both internal and external flow features, including the installation effects, and improves the prediction of the aerodynamic performance of civil aircraft equipped with engines with very high bypass ratios.

1. Introduction

Environmental and energetic constraints are reshaping the aeronautical industry, mainly due to the urge to reduce carbon-dioxide emissions and fuel consumption. New engine and aircraft designs are needed to satisfy this requirement. Among the possible new configurations, engines with increased by-pass ratio (BPR) appear to be the most valuable candidates for replacing the engines of existing aircraft in the very near future and are already replacing current engine via short-terms programs. However, reaching this high BPR leads to a major modification in the nacelle and fan design [1]. In order to increase the flow in the secondary duct, the diameter of the nacelle must be increased. In the meantime, its length is reduced to limit the weight of the engine. This reduction leads to a diminution in the air intake length that allows stabilizing the flow in front of the fan blades. In that respect, the fan is subjected to more important flow fluctuations and distortions and the classical approach where the internal flow in the engine is investigated independently from the external flow in the nacelle and the airplane is no longer feasible. Thus, all those new configurations call for a re-evaluation of design methods and the need to assess the capability of current industrial methods to model and reproduce the flow around an aircraft with engine installation. In addition, the aerodynamic performance of the engine must be computed on the complete configuration, taking into the account the installation effects and the strong interaction between the engine and the aircraft cell.

The purpose of this paper is to demonstrate the feasibility of complex simulations in an industrial framework, taking into account most of the elements of a civil transport aircraft: the wing, the fuselage, the engine pylon and nacelle, as well as the components inside the secondary flow of the UHBR engine, the rotating fan and the OGV blades (Outlet Guide Vanes), including a heterogeneous part which allows the connection with the engine pylon. The numerical simulations, adopting Unsteady-RANS approach, requires the many functionalities as for example non-coincident meshes and Chimera approach for the external part, sliding mesh and mixing planes to manage the interfaces between fixed part and rotating parts inside the engine, or radial equilibrium for the boundary conditions in the rotating frame.

The present paper will proceed as follows: a brief introduction of the selected test case is presented in section 2, describing the main characteristic of the NOVASPIRE configuration. The approach is then detailed in section 3: the grids, the Chimera technique and the handling of the interfaces between fixed and rotating parts will be presented in section 3.1, the solver characteristics as well as the approach used for simulating the configuration and analyzing steady-state, time-accurate and time averaged results will be presented in section 3.2, while section 3.3 will present the definition of the quantities used for post-processing and analyzing the results. Section 4 is entirely dedicated to the presentation and discussion of the results for each approach used: steady-state with mixing planes in section 4.1, time-accurate simulations with sliding mesh in section 4.2 and time-averaged results in section 4.3. Particular attention will be paid to the analysis of the performance of the engine, either in terms of mass-flow rates, or by looking at pressure and temperature ratios as well as at isentropic efficiencies. Section 5 will briefly present the ongoing work on a more complex configuration representing take-off conditions, where high-lift devices are also taken into the account.

DOI: 10.13009/EUCASS2023-597

2. Test case

The identified test case, named NOVASPIRE, is the result of collaboration between many European partners in the frame of the European Clean Sky 2 programme (Large Passenger Aircraft platform): it is the fusion between one of the NOVA configurations [2], the aircraft demonstrator designed by ONERA, with the ASPIRE engine [3], resulting from a previous collaboration between ONERA, Airbus, DLR and NLR [4].

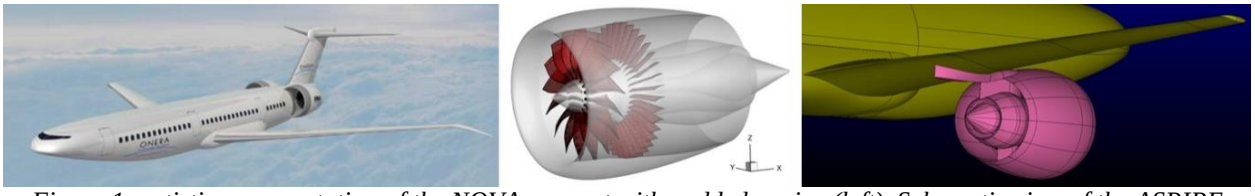

Figure 1: artistic representation of the NOVA concept with podded engine (left). Schematic view of the ASPIRE engine (centre). CAD files of the engine installed under the wing (right).

The left side of figure 1 presents an artistic representation of one the many ONERA NOVA configurations, as described in [2]. On the center of the image, a schematic view of the ASPIRE engine with all its fan and homogeneous OGV blades is presented, as investigated in EU project in reference [3]. The so called NOVASPIRE configuration is composed of the NOVA glider equipped with the ASPIRE engine. A heterogeneous OGV is inserted in the engine and links an OGV blade to the wing pylon, as represented on the right of figure 1.

Two flow conditions are presented in this work: cruise and take-off. The first simulation will be analysed in detail and corresponds to the Aerodynamic Design Point (ADP), where the plane is in its clean configuration and is in high Mach and altitude. The angle of attack is small and the engine regime is representative of stabilized cruise. The second one will be briefly discuss at the end of the article and corresponds to a low-speed and low-altitude test case. In this configuration high-lift devices are deployed, while the angle of attack as well as the engine thrust is much higher. Beside the high-lift devices, differences in the geometries of the two configurations can be seen also in the nozzle, whose diameter in take-off condition is higher in order to take into the account the greater mass-flow rate throw the engine.

3. Approach

Once some preliminary simulations are carried out on the NOVA glider, without the engine, for assisting its installation, the cruise condition configuration is meshed and then investigated using different approaches: first the so called *engine conditions*, where the ASPIRE engine is modelled with its nacelle only. Inlet/outlet boundary conditions replace the internal parts, while the fan and the OGV blades are not modelled. Then, the ASPIRE engine is completely meshed: all fan and OGV blades are included in the grid. Both steady-state simulations (RANS with mixing-plane conditions on the interfaces between internal and external parts) and time-accurate simulations (U-RANS with sliding mesh) are carried out. Because of the asymmetry of the test case, full 360° unsteady simulations are needed to reproduce the complete configuration and a few fan revolutions have to be simulated to assess the aerodynamic performance. A steady-state simulation is used to initialise the computation, where a spatial averaging on the interfaces between fixed and rotating parts is mandatory to allow the use of a local time-step. Then URANS simulations with sliding mesh are considered: a global time-stepping approach yield time-accurate results. The solutions obtained will be first briefly discussed considering both steady and unsteady results, and then a more accurate analysis will be performed on the time-averaged results. Grid and turbulence model dependency have been accurately investigated during the study, but will be discussed only briefly when discussing the engine performance.

3.1 Grid

Due to the complexity of the configuration, the mesh is composed of different structured grids created with various meshing tools and then assembled together. Each element of the NOVA glider is meshed separately with Pointwise: fuselage, wing, wingtip and wing/fuselage collar. The outer parts of the engine (nacelle and pylon) as well as the high-lift devices for the take-off configuration (inboard slat, outboard slat, flap and their cut on the wing) have been generated using ICEM-CFD, while the inner part of the engine (the fan and OGV blades, included the heterogeneous one) have been generated using Autogrid. The ensemble of inner and outer parts of the engine is a single base, composed of different structured grids, where special boundary conditions for the interfaces between the fixed and rotating parts allow for no-match connections. The main bases, 5 for the cruise condition and 11 for take-off, are then inserted in a background Cartesian grid, an additional base generated with the in-house code Cassiopée

DOI: 10.13009/EUCASS2023-597

[5]. The complete configuration is then assembled using the Chimera technique. No orphan points are obtained in all considered cases, where the blanked cells are maximized to prioritize the simulations of grid points in each base and the overlap between the different bases have been optimized to obtain the best interpolations coefficients. A schematic view of all bases but the Cartesian background is presented on the right side of figure 2. The wing grid includes a refinement in the wake of the engine in order to conserve an appropriate spatial discretization in the jet region, which is necessary for an accurate far-field exergy analysis that will be performed in the future.

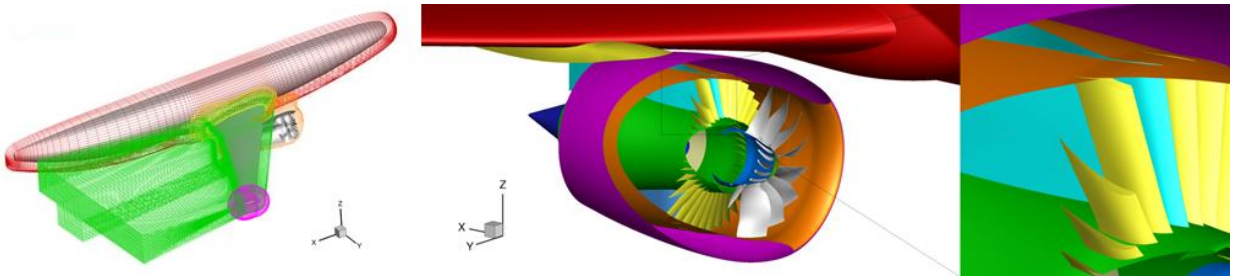

Figure 2: schematic view of the NOVASPIRE configuration with rotating fan (left). Visualisation of the internal part of the engine (centre), with a zoom on the heterogeneous OGV blade (right).

Three levels of grid refinement have been considered: a Coarse mesh, mainly used for testing the preparation of the simulation, a Medium one, which respects all the internal good practices, and a Fine one for assessing grid convergence, as will be discussed when analysing the engine performances. During the assembly, each base is split (most of the blocks are in the Cartesian background) for parallel computations. Table 1 summarizes the size of each grid investigated in cruise conditions, as well as the details of the split and the CPU time needed for each simulation, indicating the time needed for a steady-state RANS and the total time composed of one steady simulation and at least 3 fan revolutions.

Table 1: details of split strategy and CPU time for all grids

	Grid size	**Nb cores**	**Nb blocks**	**CPU time steady**	**CPU time total**
Coarse	10 M	144	831	4 h	38 h
Medium	53 M	384	1615	10 h	88 h
Fine	227 M	480	1922	26 h	230 h

The times are referred to the turbulence model k-ω with SST correction, which is the most time consuming due to his convergence. With the Spalart-Allmaras (S-A) turbulent model, the simulations are roughly 30% quicker. Results indicated that the Medium grid is considered to be sufficient to obtain satisfying results, providing that the dissipation used in the simulation is sufficiently small, which is not the case when considering the S-A turbulence model with the Roe scheme associated with the *minmod* limiter. When considering the take-off conditions, the high-lift devices are responsible for a 20% increase of grid points.

3.2 Solver

The simulations were performed with the *elsA* software (ONERA - Safran property) [6]. It solves the compressible Navier-Stokes equations on structured, unstructured and hybrid multi-block grids using finite-volume formulation. For the simulations carried out in this study, the structured capability and the Chimera approach of the solver are used. In the engine region, both mixing planes (with azimuthal averaging and radial equilibrium) and sliding mesh techniques are applied for the interfaces between fixed and rotating parts. The handling of these interfaces can be complex and need to be verified by the user, even if recent features of the *elsA* code allow for an automatic definition of the *globborder* windows that group each block face that composes the interfaces. Some of these interfaces, called *stations*, are also used during post-processing to analyse the flow conditions at different locations inside the engine. The left side of figure 3 presents a schematic view of the *stations*.

Concerning the approach adopted, the computations consist in performing firstly steady-state simulations to initialize the flow, using azimuthal averaging with radial equilibrium. Then, time-accurate URANS simulations are performed for at least 3 fan revolutions. In this case sliding mesh approach in the interfaces between fixed and rotating parts allows for a complete simulation of the configuration. Once the flow is stabilized, statistics are stored for a complete fan revolution. This approach is repeated for different turbulence models and grid levels.

DOI: 10.13009/EUCASS2023-597

The right side of figure 3 shows an example of the evolution of the mass-flow rate in the secondary stream, downstream of the OGV (*station 13* as presented on the left side of the same figure), for the Medium grid. The red line corresponds to the steady-state simulation, where the mass-flow rate quickly converges to a steady value. The green line, corresponding to the URANS simulation, shows that the solution quickly converges and periodic oscillations can be seen because of the fan rotation: 16 peaks can be noticed for each fan revolution, corresponding to a peak for each of the 16 fan blades of the engine. After 1 or 2 complete revolutions, the transient has passed and the statistics are then recorder starting from the 3rd fan revolution to obtain the time-averaged results as indicated by the dashed rectangle.

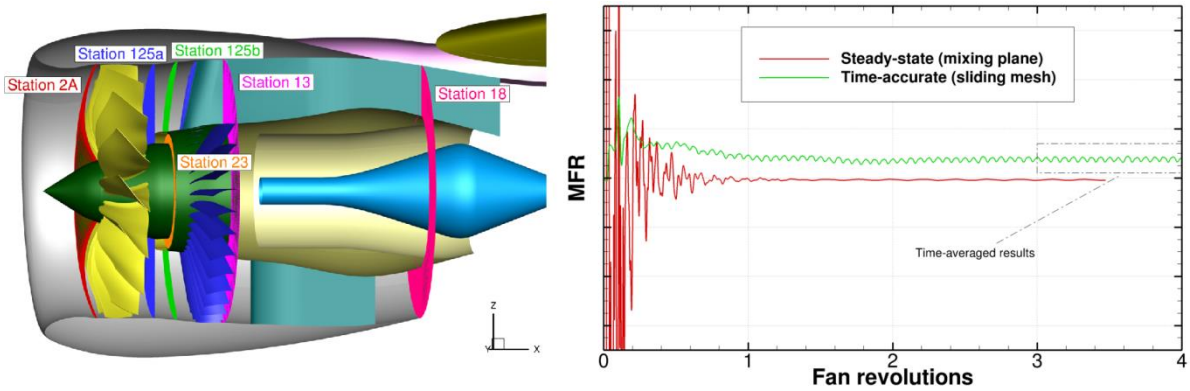

Figure 3: position and definition of the different stations used for post-processing (left). Evolution of the mass-flow rate in the secondary stream during a simulation (right).

For all grids, both S-A and k-ω turbulence models with SST corrections were investigated, considering in each case the Roe scheme with the *minmod* and the *van Albada* limiters.

3.3 Quantities for post-process

Most of the post-process and the results analysis will be based on the engine and its performance. Following ASPIRE project, different stations, defined as in figure 3, are used for computing mass-flow rates, pressure ratios, efficiencies and other 0D-parameters. Some stations are planar cuts normal to the engine axis (125a, 125b, 13 and 23), while others are either cones on either the primary or secondary flow, normal to the flow direction (stations 8 and 18, respectively), or arbitrary surfaces that follows some particular region, as station 2A upstream of the fan face.

Table 2: definition of the 0D parameters used for performance evaluation.

Acronym	Parameter	Definition
FPR	Fan Pressure Ratio	Pt13/Pt2A
FTR	Fan Temperature Ratio	Tt13/Tt2A
η_{Fan}	Fan stage Isentropic Efficiency	$(FPR^{(\gamma-1)/\gamma}-1)/(FTR-1)$
RPR	Rotor Pressure Ratio	Pt125a/Pt2A
RTR	Rotor Temperature Ratio	Tt125a/Tt2A
η_{Rot}	Rotor stage Isentropic Efficiency	$(RPR^{(\gamma-1)/\gamma}-1)/(RTR-1)$
CPR	Core Pressure Ratio	Pt8/P0
FNPR	Fan Nozzle Pressure Ratio	Pt13/Pt0
MFR	Mass-Flow Rate	-

Starting from the definition of the stations, one can derive all coefficients that can be used to assess the performance of the engine. However, as it will be explained in section 4.3.3, those coefficients will be normalized using a reference and their absolute values will not be shown, for brevity and confidentiality reasons. Table 2 presents a summary of those parameters with their definition based on the stations, where Pt and Tt are the total pressure and total temperature and the subscript indicates the station where the value has been taken. For all types of

DOI: 10.13009/EUCASS2023-597

simulations, a spatial averaging on the surface, weighted by the mass-flow rate of each station, is performed to integrate and obtain the desired quantities in each location. The table also presents the fan and rotor stage isentropic efficiency, that can be derived from the 0D parameters using the definition on the right column.

4. Results: cruise conditions

This section presents all the results of the simulations performed with the different approaches, on all grids and with different turbulence models and numerical schemes. Each section focuses on a specific aspect, while the majority of the results are discussed for the solution obtained when performing a time average of URANS results with sliding mesh, considered the most accurate and reliable approach to evaluate the performance of the configuration (time-averaged results presented section 4.3).

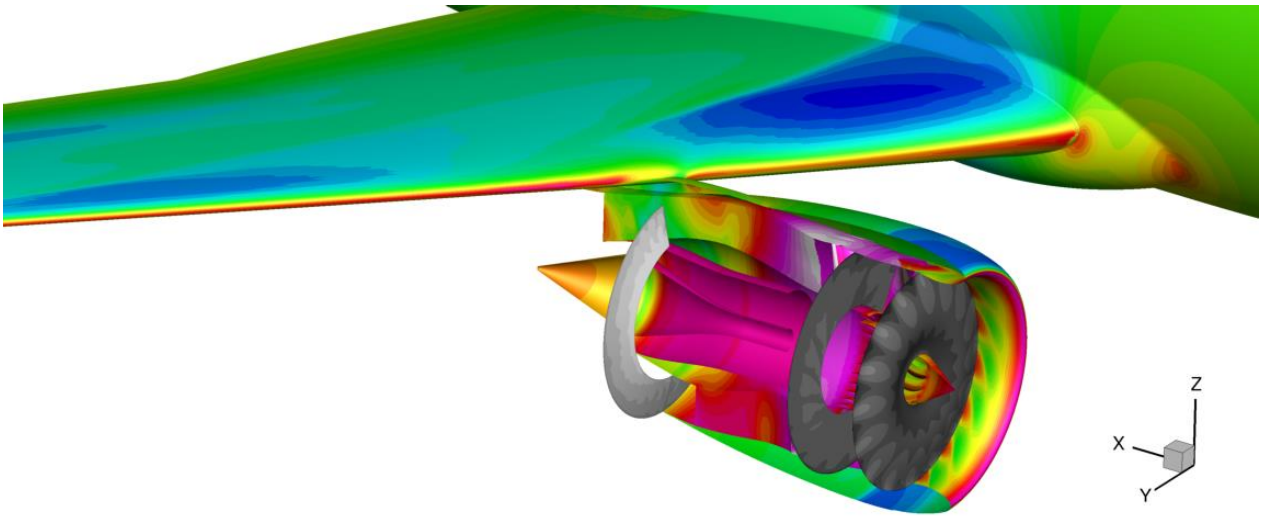

Figure 4: visualisation of the complete configuration coloured by wall-pressure distribution and Mach number distribution on stations 2A, 125b and 18 inside the engine (greyscale).

Figure 4 presents a typical result of the simulation, where the solution is presented for both the external flow outside of the nacelle and the internal flow developing in the engine. Low values of pressure distributions indicate a supersonic region on both the suction side of the wing and the external part of the nacelle, while the abrupt increases of pressure imply the presence of multiple shock waves. The internal flow is much more complex and will be the focus of the analysis in the next sections. The solution will be especially investigated in the stations defined before and presented in figure 3, highlighted by a greyscale distribution of Mach number in figure 4.

4.1 Steady-state simulations

Despite the unsteady features of the flow, the configuration can also be considered using a steady approach. In this case, a local time stepping is adopted for the temporal scheme, and the interfaces between fixed and rotating parts are azimuthally averaged using the so-called *mixing-planes.* The main reason why these simulations are performed is to have a quick evaluation of the flow field as well as an appraisal of the engine performance. These simulations are also used to verify the convergence of the solution, especially in terms of mass-flow rates in the engine, as for example in the boundary condition with valve law, downstream of the splitter (in correspondence of station 23), where a constant mass-flow rate is imposed with radial equilibrium. Despite the complexity of the configuration, the mixing-plane approach allows to obtain a satisfying solution, even after the azimuthal averaging, with few resources: results are obtained in a tenth of the time needed to run a complete URANS simulation with multiple fan revolutions.

After validation, the result thus obtained is used to initialize the time-accurate simulation. Starting from a steady-state solution allows for a shorter transient, yielding a faster convergence of the time-accurate simulation, thus a cheaper and quicker simulation.

Even if the steady-state approach can easily provide a solution without the need of a time-resolved simulation, the spatial averaging introduced by the mixing planes between fixed and rotating parts has important consequences on the flow-field and, as it will be discussed later, impacts the global performance of the engine.

DOI: 10.13009/EUCASS2023-597

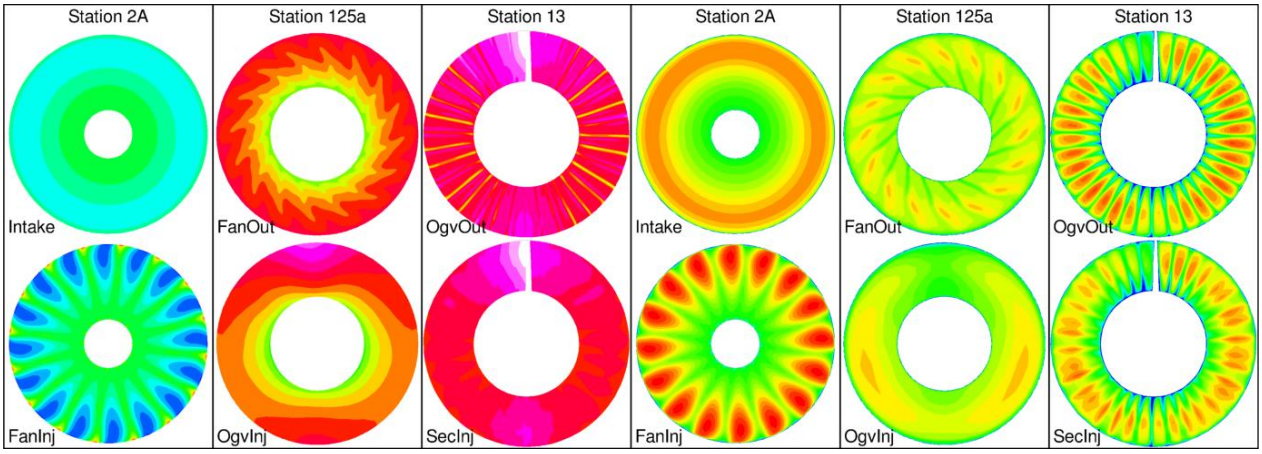

Figure 5: pressure (left) and axial velocity (right) distribution on the three interfaces between intake-fan, fan-OGV and OGV-secondary stream. The upper disks represents the flow-field upstream the interface, the lower disks downstream.

Figure 5 allows for visualizing this feature by presenting the pressure distribution on the left and the velocity distribution on the right in correspondence of the three interfaces where mixing planes or sliding mesh are (Medium grid, S-A turbulence model and *minmod* limiter is presented). The top of the image presents the flow-field upstream of each interface, while the bottom of the image presents the downstream one. When comparing *Intake* with *FanInj*, located roughly where the station 2A is, one can see that on the intake side (fixed frame in the nacelle grid) the flow does not present any information about the fan blades: the pressure or velocity variations due to this rotating parts are azimuthally averaged and the only asymmetric effect that can be seen is due to the flow-field distortion because of the angle of attack and the droop angle of the nacelle. Contrarily, when looking at the distribution of the *FanInj* interface, in the rotating frame of the engine grid, the effect of the fan blades can be clearly seen. However the flow distortion is not present anymore since all asymmetry has been averaged during the radial equilibrium. In cruise conditions, the boundary layers in the nacelle are thin, so the spatial average has little impact on the solution. Nonetheless, if the angle of attack were higher, a flow-separation could have been present in a given position of the intake, which would then have been averaged with the flow in the other azimuthal locations of the intake. The flow entering the fan would thus have been unphysical, with thick and uniform boundary layers.

Still focussing on figure 5, a similar behaviour can be observed when the flow passes between the rotating fan (interface called *FanOut*) and the fixed OGV (interface called *OgvInj*), which happens near the station 125a. In this case the rotating frame is in the upstream plot: the trace of the fan-blade wake can be seen in both pressure and velocity distribution, but the mixing plane between the two interfaces is responsible once again for a spatial average. The flow downstream the interface is however not symmetrical, because of the heterogeneous OGV and the bifurcation on the lower part of the nacelle, whose effects are visible even upstream the OGV stage.

Finally, figure 5 presents also the interface between the OGV (interface called *OgvOut*) and the secondary stream in the nozzle (called *SecInj*), located near station 13. This interface intercepts the heterogeneous OGV blade, as can be noticed by the fact that a wall is present on the top of the interface. Contrarily to the previous interfaces, this region is composed by two grids that, even if they belong to different bases and do not match, both are in the fixed frame: the mixing plane with spatial averaging is not needed even for the steady-state simulation. A sliding mesh technique can be used, and the information is simply interpolated between the interfaces. In the example of figure 5, the medium grid with the S-A turbulence model and the *minmod* limiter is used. As it will be discussed later, this combination of turbulent model and numerical scheme is very dissipative, as can be noticed by the pressure and velocity loss that can be observed in the contour maps. When considering a finer grid or a less dissipative limiter, the sliding mesh approach on two fixed grids do not cause significant dissipation, as can be seen in figure 8 or figure 10 in correspondence of station 13.

4.2 Time-accurate simulations

The sliding mesh technique presented in this section allows avoiding any spatial averaging between the interfaces of fixed and rotating grids. A time-accurate simulation is needed, so the temporal scheme of the solver is changed from *backward Euler* to *Gear* and a global time stepping is used. Based on the lesson learnt during the ASPIRE project, the selected time step is particularly small and very few inner iterations are needed for converging each time step. A time-step convergence study has also been performed and confirmed that for the *elsA* solver it is more convenient to perform, for each fan revolution, a large number of small steps rather than fewer big ones, that would oblige to perform more inner-iterations to converge and often leads to unstable results [7]. The time-step size used is

DOI: 10.13009/EUCASS2023-597

approximately 5e-6 seconds, corresponding almost 6000 steps per fan revolution. This value has been found by multiplying by a factor of 10 the number of fan blades times the number of OGV blades and is kept the same for all grid refinements and turbulence models. Depending on the grid level, the turbulence model and the numerical scheme, between 5 and 12 inner iterations are needed to reach the convergence criterion of each time step. A typical single fan revolution is thus simulated with roughly 60000 total iterations.

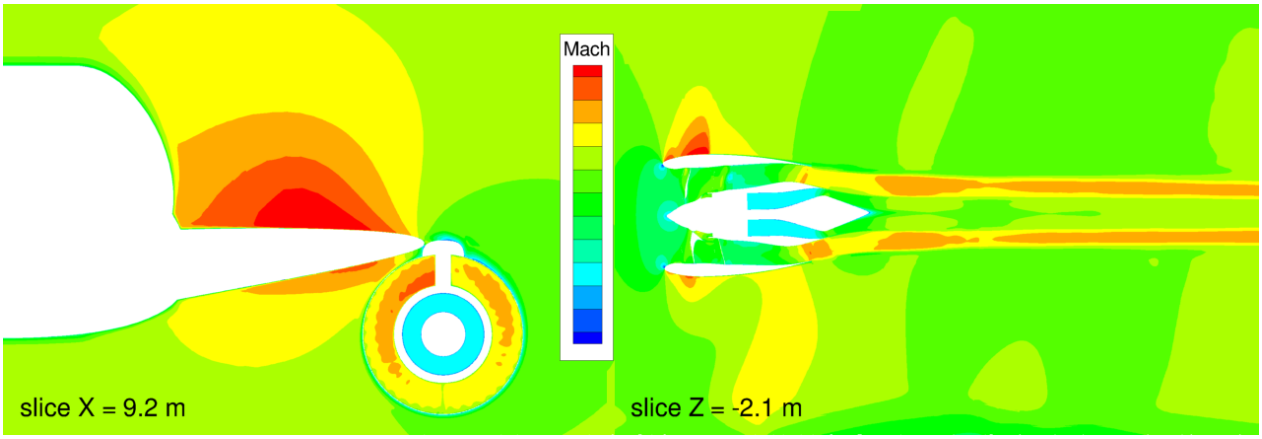

Figure 6: Mach number distribution on a vertical and horizontal cutting plane in correspondence of the engine. Instantaneous result on the Fine grid, k-ω turbulence model and van Albada limiter.

The results obtained with this approach are time-resolved: this section presents the solution at the last iteration of the simulation, after the transient and once the flow has stabilized. The right side of figure 3 presented the evolution of the mass-flow rate during such simulations, where it can be seen that the flow quickly converges to a regime where periodic variations of the flow quantities can be observed due to the rotation of the fan blades: every one of the 16 peaks per each fan revolution on the green line corresponds to the passage of the 16 fan blades.

Figure 6 presents an instantaneous visualisation of the Mach number distribution on two cuts of the solution obtained. The left side presents a vertical cut, normal to the engine axis, downstream of the OGV. Supersonic regions can be observed not only on the wing, but also inside the engine, especially inboard of the bifurcation. Focusing inside the nozzle, the secondary stream presents some flow variation due to the wake of each of the 36 OGV blades and a flow asymmetry due to the rotating fan: in the case of a steady-state solution the flow would have been much more uniform, not only because of the temporal average introduced by the local time step, but also because of the spatial averaging of the mixing planes.

The right side of figure 6 presents a horizontal cut of the solution in correspondence of the engine axis. The Mach number distribution indicates that the flow is not symmetric due to the toe-in angle of the nacelle. The yellow zone on the inboard of the nozzle corresponds to a region where the flow accelerates because of the proximity to the wing and the obstruction of the fuselage. In the secondary stream, the flow is choked and a sonic throat can be observed on each side of the nozzle, close to the trailing edge of the outer fan surface (OFS). Downstream of the engine, the wake of the jet stream is visible, with a low dissipation due to a grid refinement in this region, as indicated on the left side of figure 2.

Since the most complex part of the flow is located inside the engine, the discussion will focus hereafter on this region. A convenient way for analysing the results inside the nacelle is by looking at an isosurface of constant radius, as presented in figure 7. This circular cut presents the total pressure ratio (top) and the Mach number distribution (bottom) at 0.9 m from the engine axis. Starting from the left side of the images, the surface intersects the fan blades, then the OGV blades, where the heterogeneous one can clearly be seen, while the lower bifurcation appears in white on the background. Moving downstream (towards the right of the image), the surface intersects the asymmetric engine pylon.

From the total pressure distribution of figure 7 one can easily understand that the plot presents a snapshot of the time-accurate simulation, thus an instantaneous result of the URANS solution: the wake of each fan an OGV blade is visible and is passing through the interfaces between fixed and rotating parts. The interaction between the wakes of the fan blades with the OGV ones is also visible from the total pressure distribution. Flow unsteadiness is mainly due to the rotation, but also due to flow separation that can be confirmed by the blue regions, indicating total pressure loss.

The Mach number distribution is presented on the lower side of figure 7: the red zone inboard of the heterogeneous OGV blades indicates a supersonic region in the nozzle throat, which is more extended on the left side of the nozzle, as observed while discussing figure 6. A separated zone is then visible both downstream of the heterogeneous OGV blades and the engine pylon, indicating that the engine integration could be modified in order to

DOI: 10.13009/EUCASS2023-597

optimize the design for the considered flow condition. This flow separation can also be observed on the pressure side of the wing, as in figure 9, where the external part of the pylon indicates a flow separation in its aft part.

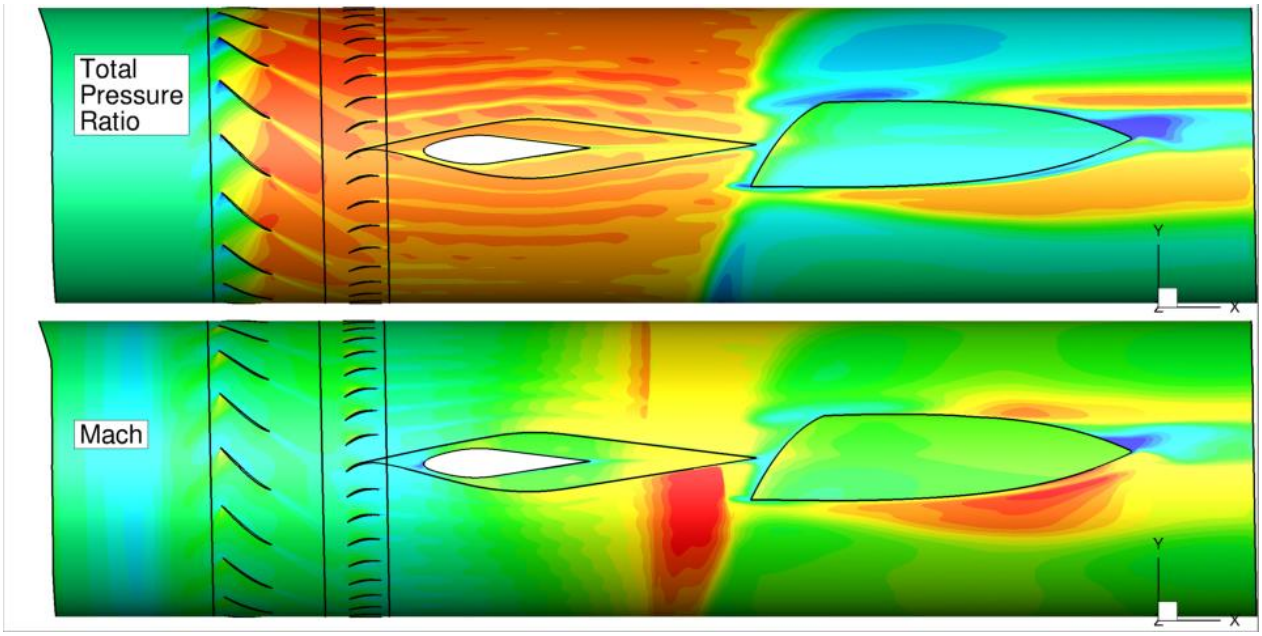

Figure 7: iso-surface of constant radius cutting through the blades and the nacelle pylon. Result obtained on the Fine grid using the S-A turbulence model.

To discuss the results inside the engine, we hereafter consider the three most important stations, whose definitions are on the left side of figure 3: station 2A, upstream of the fan, station 125b between the fan and the OGV and station 13, downstream the OGV blades. The distinction between the upstream and downstream boundaries of an interface separating fixed and rotating grids, as presented for the steady-state results, is now useless, since the results presented in this section and in the next one have been obtained using a sliding mesh technique, where the two interfaces have the same information.

Figure 8 shows the contour maps at the end of a time-accurate simulation for different flow variables. On the top left of the figure, the pressure distribution is very similar to what obtained in the steady state simulation, with the important difference that now the asymmetry of the flow is clearly visible in all stations: on 2A, the pressure between the blades on the top right side of the station is higher than the pressure between the blades on the bottom left side of the station. This is due to the obstruction of the heterogeneous OGV blade that interferes with the flow. This obstruction causes an increase of pressure that is clearly visible in station 13, in a similar way as the trace of the lower bifurcation causes a pressure increase on the bottom of the image.

Moving towards the right of figure 8, still on the first row, pressure stagnation distribution shows that the fan is responsible for a great increase of the average value of pressure stagnation: although absolute values are hidden for confidentiality reasons, the colormap indicate a pressure rise in agreement with the expected FPR. No particular signs of total pressure losses are visible besides the wake of the OGV blades, responsible for the 36 radial lines in station 13.

When focusing on the second row of figure 8, the Mach number distribution presents a colourful plot that confirms what observed above when discussing the pressure fields. From station 13 of this plot is however more evident that the flow past the OGV blades has a higher speed on the sides of the nozzle, where no obstructions are present, than on the upper and lower parts, where the bifurcations are slowing down the flow. Still on the same row of the figure, the temperature stagnation distribution allows to quantify the increase of the temperature due to the work performed by the fan.

The last row of figure 8 shows the swirl and the turbulent viscosity ratio (hereafter μ_t/μ). From the first quantity (left side of the image) one can immediately see that the fan is obviously responsible for a great increase of the swirl, but the OGV blades are efficiently straightening the flow and bringing the value to zero, associated with the blue colour, with the exception of the region near the heterogeneous OGV blade, surely because of the obstruction of the bifurcation downstream.

Finally, the turbulent viscosity, presented with a logarithmic colormap on the bottom right of figure 8, shows that the flow is entering into station 2A with a very low turbulence, except in the boundary layers in the fan shroud and the spinner. In station 125b, the increase of turbulence caused by the fan is evident; however the flow keeps low values of turbulent viscosity ratio in between two fan blades. Downstream of the OGV stage, high values of turbulence are visible everywhere, in particular in the wake of the blades with a thicker shear layer.

DOI: 10.13009/EUCASS2023-597

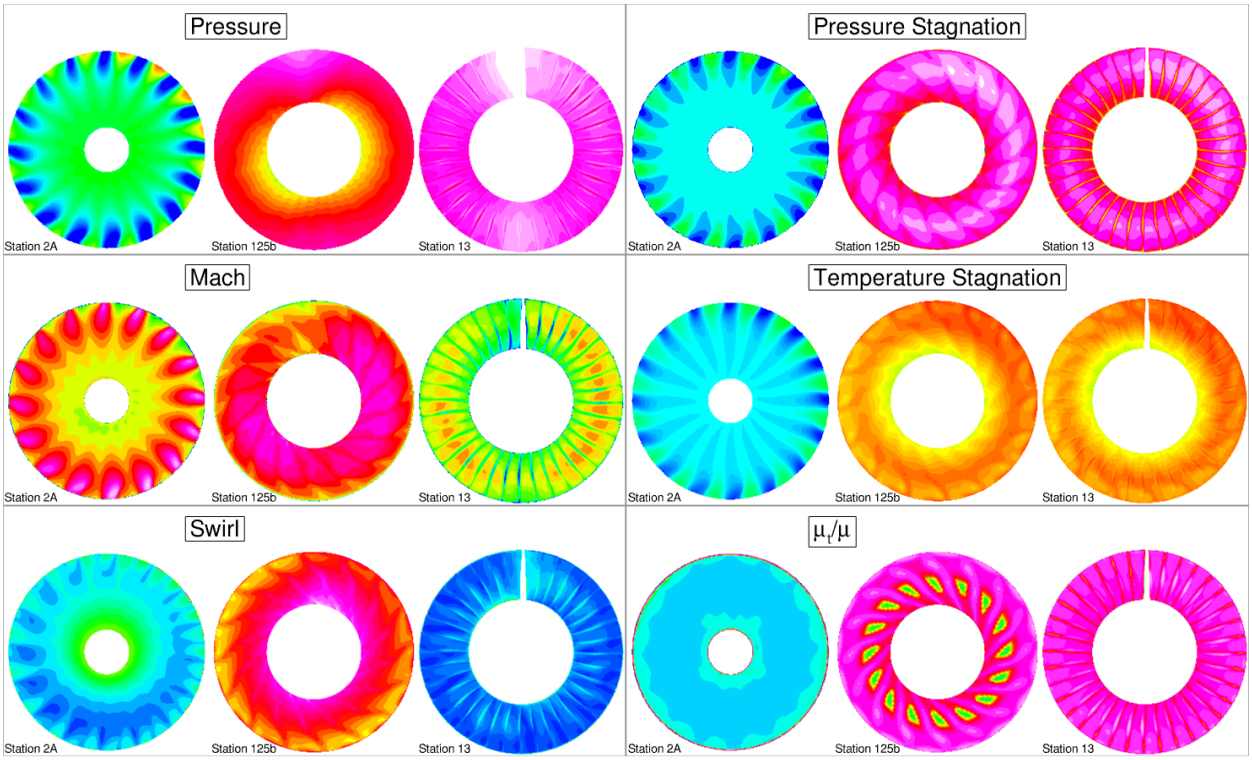

Figure 8: contour maps with different variables in stations 2A (upstream of the fan), 125b (between fan and OGV) and downstream the OGV. Instantaneous results of a time-accurate simulation, Fine grid, k-ω van Albada.

It is important to remember that the results just discussed are instantaneous results referred to a particular moment of the simulation. Different plots can be observed if extracting a solution at a different moment, corresponding to a fan position rotated with respect to the one just analysed.

4.3 Time-averaged results

Once the flow is completely established in the engine, flow statistics can be extracted for a more accurate analysis of the solution. This section presents a discussion of different quantities, illustrated section by section, and referred to the time-accurate solution averaged over one complete fan revolution. The Fine gird with the k-ω SST model is considered, if not specified differently.

4.3.1 2D Contours

The two sides of figure 9 present the lower and upper wall-pressure distribution on the whole configuration. On each image, streamtraces following the components of the skin-friction coefficient indicate the flow direction and highlight the presence of separations and stagnation points.

As discussed when analysing the results of the steady-state simulations presented in figure 4, supersonic regions are present both on the suction side of the wing and around the nacelle. The streamtraces on the right side of figure 9 clearly show the separation on the outboard side of the engine pylon: this separation is associated with an increase of the wall pressure of the wing downstream of the engine and could be suppressed or at least reduced with an asymmetrical pylon or a different toe angle of the engine installation.

The suction side, visible on the right of figure 9, indicates that the engine has a large impact on the pressure distribution of the wing, surely due to the proximity of the nacelle, which is greater than in classical configuration with lower by-pass ratio due to the very large diameter of this UHBR engine.

Similarly to what discussed for instantaneous results in figure 8, results on the stations for the time-averaged results are presented in figure 10. Significant differences can be seen in station 2A, where the time-average in the fan region significantly changed the distributions of all quantities. The local effect of each single fan blade is not visible anymore.

DOI: 10.13009/EUCASS2023-597

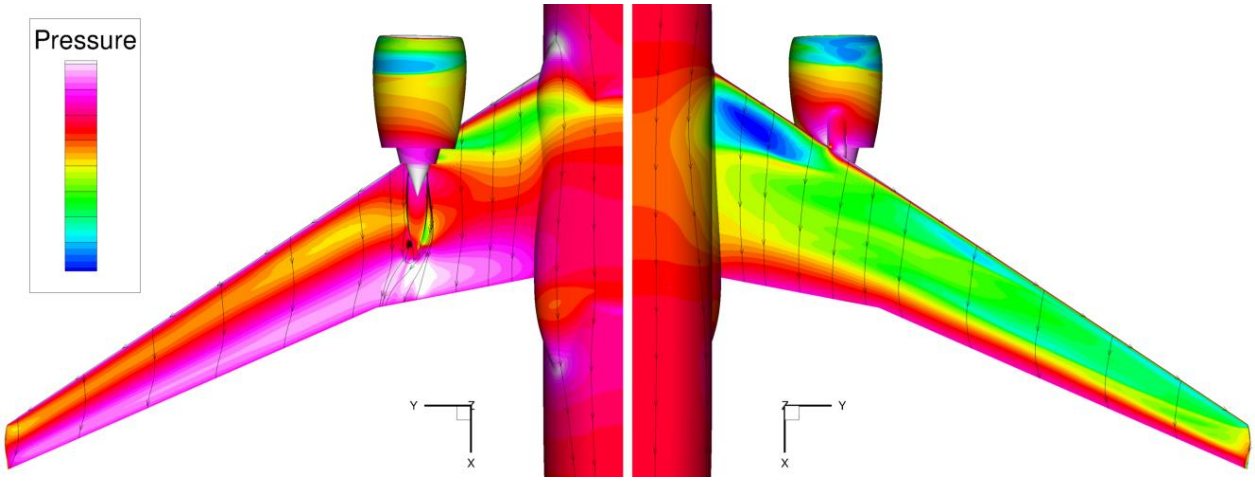

Figure 9: pressure distribution on the lower and upper side of the configuration. Fine grid, k-ω SST, van Albada..

However, thanks to the average, it is easier to observe the distortions on the fan face, responsible for flow acceleration on the lower part of the intake due to the angle of attack of the incoming flow: lower static pressure and higher Mach number can be observed. In the fan region total pressure and temperature distribution are now uniform.

In figure 10, the distributions on station 125b are very similar to those of figure 8 (instantaneous result of time-accurate simulations): the same comments apply for most of the plots presented in the two figures. However, in the case of time-averaged results, local unsteadiness are no longer visible and smoother results can be observed. In addition, focussing on the distribution of the turbulent viscosity ratio, it is no longer possible to observe the wake of each fan blade individually and it is clear that the turbulent viscosity globally increases because of the rotating fan.

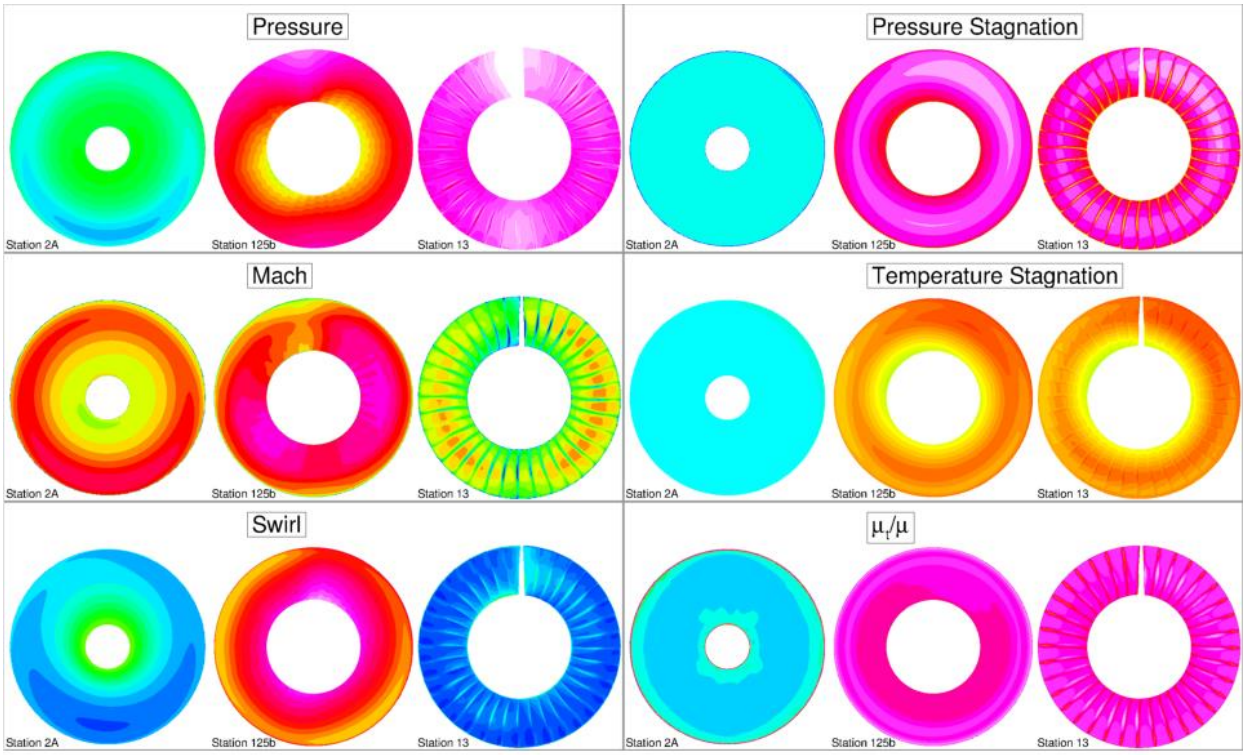

Figure 10: contour maps with different variables in stations 2A (upstream of the fan), 125b (between fan and OGV) and downstream the OGV. Time-averaged result of a time-accurate simulation, Fine grid, k-ω SST, van Albada.

Finally, the distributions on station 13, downstream of the OGV, are almost identical to those of figure 8, since in this region the effect of the rotating fan is compensated by the effect of the OGV. However, contrarily to steady-state results presented in section 4.1, the flow is not symmetric and the effect of the heterogeneous blade can for example be seen on the top right corner of the figure, where higher pressure stagnation can be seen on both stations 125b and 13 in correspondence of the top right part of the station.

DOI: 10.13009/EUCASS2023-597

4.3.2 1D distributions

Wall-pressure distribution can be visualised in contour maps as in figure 9 or presented in 1D plot by defining cutting planes as in figure 11. Vertical cuts on the wing can give information about Cp distributions on the plane, while horizontal cuts on a specific fan blade can give an appraisal of Cp distributions inside the engine as for example in the locations specified on the right side of figure 11.

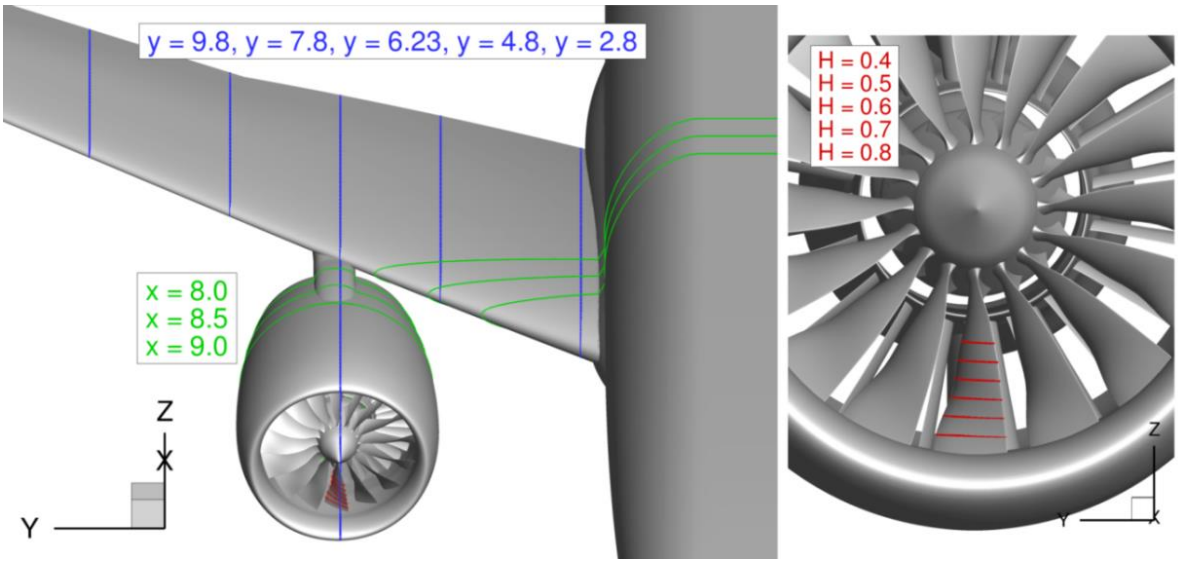

Figure 11: location of the main cutting planes for Cp comparison.

Figure 12 presents the Cp distributions on the wing for four span-wise locations. Different grids and models are presented on the same plot, indicating very small dependency to grid density and CFD parameters. Regardless of the grid level, in the most inboard part of the wing an abrupt increase of Cp indicates the presence of the shock wave close to the fuselage. When moving towards the wing-tip, the pressure distribution becomes more uniform, and finally two shock waves can be seen in the most outboard part of the wing.

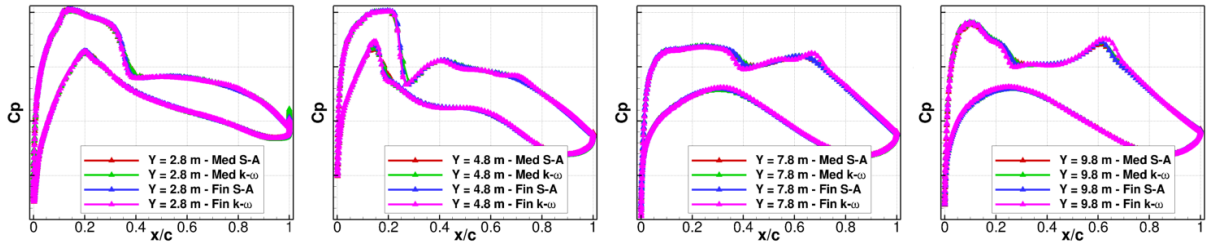

Figure 12: pressure coefficient distributions on the wing at different span-wise locations for different turbulence models and grid-refinement levels. From left to right: y = 2.8 m, y = 4.8 m, y = 7.8 m and y = 9.8 m.

The Cp distribution on the lower fan blade is presented in figure 13 for different channel height locations (H). Starting from the top left of the figure, lower H indicate the proximity of the fan hub. In this region the flow is subsonic and after a small deceleration on the suction side of the blade downstream of the stagnation point, the pressure constantly increases up to the trailing edge.

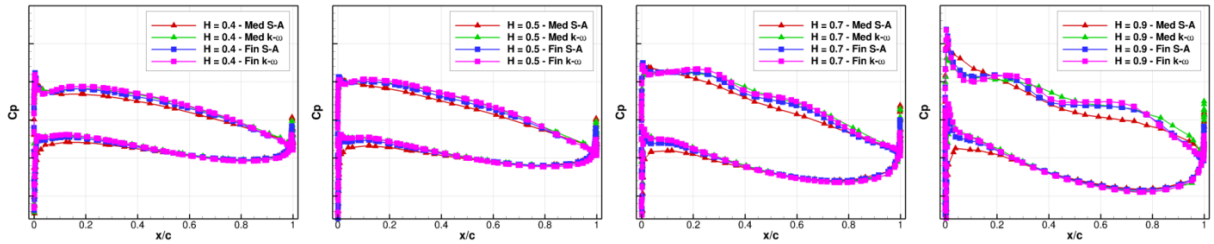

Figure 13: pressure coefficient distributions on the lowest fan-blade at different span-wise locations for different turbulence models and grid-refinement levels. From left to right: H = 0.4, H = 0.5, H = 0.7 and H =0.9.

DOI: 10.13009/EUCASS2023-597

Similar behaviour is observed up to H = 0.5, but starting from H = 0.7 some oscillations begin to appear on the suction side of the blade. The effects of grid and turbulence model are slightly more visible. However, a part from the red line, corresponding to the Medium grid, Spalart-Allmaras with Roe scheme and *minmod* limiter, the results converge to a solution that indicates an acceleration and deceleration of the flow in the proximity of the fan tip.

4.3.3 Integrated values

The quantities for performance evaluation defined in section 3.3 are briefly presented. For confidentiality reasons, results will not be discussed using their dimensional unit, but they will be normalized using the time-averaged results obtained on the finest grid using the k-ω SST model, *van Albada* limiter, considered the most accurate result. The next tables present, for each quantity, the error with respect to the reference when considering a result obtained with a given approach (steady-state, time-accurate or time-averaged), or a given grid (Coarse, Medium or Fine), or a given turbulence model (S-A or k-ω SST) and limiter (*minmod* or *van Albada*). All combinations plus some additional models have been tested during the work, but only the main conclusions will be presented here.

Table 3 presents the summary of the mass-flow rates in all stations, following the definitions available on the left side of figure 3. The results have been obtained using the medium grid, S-A turbulence model and Roe scheme with *minmod* limiter, and the table compares the mass-flow rates obtained with the steady-state simulations, the time-accurate and the time-averaged. Overall, all approaches yield similar results. However, the mass flow-rates is systematically underestimated (negative values in all table cells), because of the use of the Medium grid. Nonetheless, the difference always stays in the limits of 1%, which is still considered acceptable. No big differences can be observed while comparing an instantaneous result of the time-accurate simulation and the time-averaged ones.

Table 3: error on the mass-flow rates obtained on the Medium grid with different approaches with respect to the reference (time-averaged values, Fine grid). For all cases: k-ω SST model, van Albada limiter).

	2A	**125a**	**125b**	**13**	**8**	**23**	**18**
Steady-state	-0.37%	-0.39%	-0.78%	-0.93%	-0.10%	-0.62%	-0.81%
Time-accurate	-0.43%	-0.48%	-0.61%	-0.79%	-0.21%	-0.64%	-0.69%
Time-averaged	-0.45%	-0.48%	-0.64%	-0.77%	-0.21%	-0.85%	-0.69%

Regardless the approach adopted, some small losses can be observed when moving from one station to another that is supposed to have the same mass-flow rate because of the conservation of mass. For example, stations 2A and 125b are located just upstream and downstream of the fan, so they are supposed to have identical MFR. However a difference around 0.2% can be observed. With dimensions, this will correspond to a loss of approximately 1 kg/s. Similarly, a loss of up to 0.1% can be observed between stations 125b, 13 and 18, located in the secondary stream. The interfaces with mixing planes or sliding mesh are responsible for those losses, which as will be discussed in Table 5 are decreasing when refining the grid.

Table 4 presents the same approach comparison as in table 3, but focussing on the 0D parameters computed, according the definition in table 2, by performing an integration of the spatial average of the considered surface, weighted by the mass-flow rate of each station. The values obtained by the different approach are almost identical to each other, confirming that the steady-state solution is already a valuable approach to analyse the performances. However, higher absolute values indicate some discrepancy between the results on the table, obtained on the Medium grid using the *minmod* limiter, and the reference, obtained on the Fine grid with the less dissipative *van Albada* limiter. In the case of the isentropic efficiency, especially for the one referred to the fan, the error with respect to the reference can go up to 5%. Negative values indicate once again that the Medium grid tends to underestimate most of the quantities, probably due to the grid dissipation which is higher on coarser grids.

Table 4: error on the 0D parameters rates obtained on the Medium grid with different approaches with respect to the reference (time-averaged values, Fine grid). For all cases: k-ω SST model, van Albada limiter.

	FPR	**FTR**	**η_{Fan}**	**RPR**	**RTR**	**η_{Rot}**	**CPR**	**FNPR**
Steady-state	-0.81%	0.16%	-5.15%	0.07%	0.18%	-2.03%	-0.72%	-0.09%
Time-accurate	-0.67%	0.18%	-4.88%	0.02%	0.18%	-2.17%	-0.62%	-0.09%
Time-averaged	-0.60%	0.13%	-4.04%	0.06%	0.14%	-1.51%	-0.62%	-0.09%

DOI: 10.13009/EUCASS2023-597

Still in table 4 one can observe that steady-state results usually present a greater error, while time-accurate and time-averaged ones are very similar. The differences remain however small in all pressure and temperature ratios, never exceeding 1%.

Since the tested approaches lead to very similar results, the next tables will assess the grid and model dependency. Time-accurate results are presented in tables 5 and 6, showing as before the error with respect to the time-averaged results on the Fine grid, using k-ω turbulence model and *van Albada* limiter. For the medium grid only, all 4 combinations of turbulence model and numerical scheme are presented.

Table 5: error on the mass-flow rates obtained on different grids and turbulence models, with respect to the reference (time-averaged values, Fine grid). For all cases: time-accurate results.

	2A	**125a**	**125b**	**13**	**8**	**23**	**18**
Coarse, S-A, *minmod*	-5.04%	-5.29%	-5.65%	-5.83%	-1.12%	-1.61%	-5.78%
Coarse, k-ω, *van Albada*	-3.36%	-3.79%	-4.11%	-4.19%	-0.24%	-2.12%	-4.18%
Medium, S-A, *minmod*	-3.05%	-3.09%	-3.41%	-3.54%	-0.39%	-0.54%	-3.44%
Medium, k-ω, *minmod*	-2.33%	-2.36%	-2.59%	-2.72%	-0.29%	-0.57%	-2.62%
Medium, S-A, *van Albada*	-1.96%	-2.03%	-2.32%	-2.52%	-0.17%	-0.62%	-2.47%
Medium, k-ω, *van Albada*	-0.43%	-0.48%	-0.61%	-0.79%	-0.21%	-0.64%	-0.69%
Fine, S-A, *minmod*	-0.96%	-0.97%	-1.04%	-1.06%	-0.16%	-0.09%	-1.06%
Fine, k-ω, *van Albada*	0.02%	0.01%	0.01%	0.01%	-0.07%	-0.12%	0.00%

In terms of mass-flow rates (table 5) one can clearly see that the Coarse grid has the greatest errors (up to 6% when using the more dissipative *minmod* limiter). The error is lower when considering the Medium grid and the lowest in the case of the Fine grid. The last line of the table shows the discrepancy on the Fine grid when comparing time-accurate results to time-averaged ones (the reference): the error never exceeds 0.12%.

Two interesting remarks can be made concerning the limiters: regardless the turbulence model, the *van Albada* limiter yields a more accurate result than the *minmod*. Interesting, when coupled with the k-ω SST turbulence model, the Medium grid with *van Albada* limiter yields a result as precise as the Fine grid coupled with the *minmod* one. This behaviour is confirmed also by the 0D parameters presented in table 6 and is seen as a confirmation that satisfying grid convergence is achieved, provided that the numerical scheme is not too dissipative.

Table 6: error on the 0D parameters obtained as in table 5.

	FPR	**FTR**	**η_{Fan}**	**RPR**	**RTR**	**η_{Rot}**	**CPR**	**FNPR**
Coarse, S-A, *minmod*	-4.51%	0.10%	-19.19%	-2.95%	0.11%	-12.75%	-4.74%	-1.33%
Coarse, k-ω, *van Albada*	-3.18%	0.14%	-14.22%	-2.11%	0.14%	-9.84%	-3.36%	-0.72%
Medium, S-A, *minmod*	-3.11%	0.01%	-12.63%	-1.45%	0.02%	-5.86%	-3.12%	-0.36%
Medium, k-ω, *minmod*	-2.44%	0.07%	-10.52%	-1.01%	0.07%	-4.75%	-2.45%	-0.31%
Medium, S-A, *van Albada*	-2.34%	-0.01%	-9.18%	-1.15%	-0.02%	-4.23%	-2.31%	-0.14%
Medium, k-ω, *van Albada*	-0.67%	0.18%	-4.88%	0.02%	0.18%	-2.17%	-0.62%	-0.09%
Fine, S-A, *minmod*	-0.99%	0.01%	-4.02%	-0.69%	0.00%	-2.64%	-0.91%	-0.11%
Fine, k-ω, *van Albada*	-0.11%	0.07%	-1.33%	-0.09%	0.06%	-1.13%	0.01%	0.03%

As in the case of table 4, the 0D parameters have a larger discrepancy than the mass-flow rates. Once again, the errors presented in the tables are the highest for the isentropic efficiencies, where values up to 19% are visible for the coarsest grid with the most dissipative scheme. However the errors decrease when considering a finer grid and a less dissipative scheme, and as in the previous case, the Medium grid with *van Albada* limiter is as accurate as the Fine grid with the *minmod* one. Finally, it can be seen that the fan and rotor isentropic efficiency are very sensitive to the results, since an error of roughly 1% is observed when comparing time-accurate with time-averaged results.

DOI: 10.13009/EUCASS2023-597

5 Results: take-off conditions

This section will briefly present the ongoing work on take-off conditions, where high-lift devices have been designed and integrated in the configuration. One flap and two slats have been included, with a deployment of 12° and 10° respectively. These elements are added using the Chimera technique, allowing for a versatile switch between the configurations while keeping most of the other elements.

Figure 14 present a detailed view of the grid assembly with in red the same wing grid used in cruise conditions, plus the blanking grid for taking into the account the local wing modification (magenta grid for the slat, green grid for the flap) and the element itself (yellow for the slat, blue for the flap). Overall, the grid is now composed of 12 bases: 4 bases for the glider as in cruise conditions, one for the engine that besides some minor geometry modification is identical to the previous case, plus 6 grids for each of the high-lift elements and their blanking bodies. The Cartesian background, automatically generated using Cassiopée, is adapted to take into the account the high-lift devices. The total grid size is 11M for the Coarse, 62M for the Medium and 280M for the Fine grid.

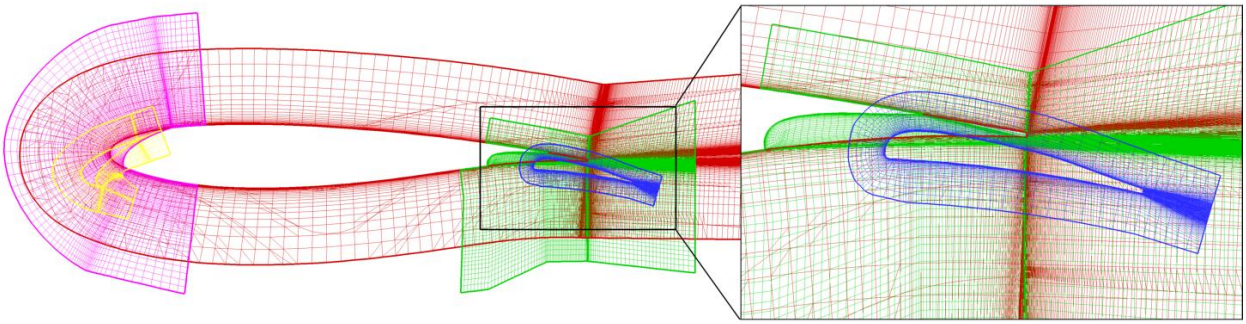

Figure 14: chimera assembly of the high-lift devices on the wing.

A part from the difference in the geometry, the boundary conditions are obviously adapted to represent take-off conditions. Not only Mach number and the altitude are lower, but the fan rotation and the total state representing the primary stream are adapted for the higher mass-flow rate configuration. The approach adopted is however strictly identical: first steady-state simulations are performed using mixing planes with radial equilibrium in the interfaces between fixed and rotating parts, then time-accurate simulations are performed and time-average solutions are analysed once the flow field is established.

Despite the much higher angle of attack, the flow remains attached inside the engine, due to the aspiration effect of the engine. Much stronger interactions between the intake and the rotating fan are observed inside the nacelle, while on the plane the flow has the typical pressure and velocity distribution of a wing in take off conditions.

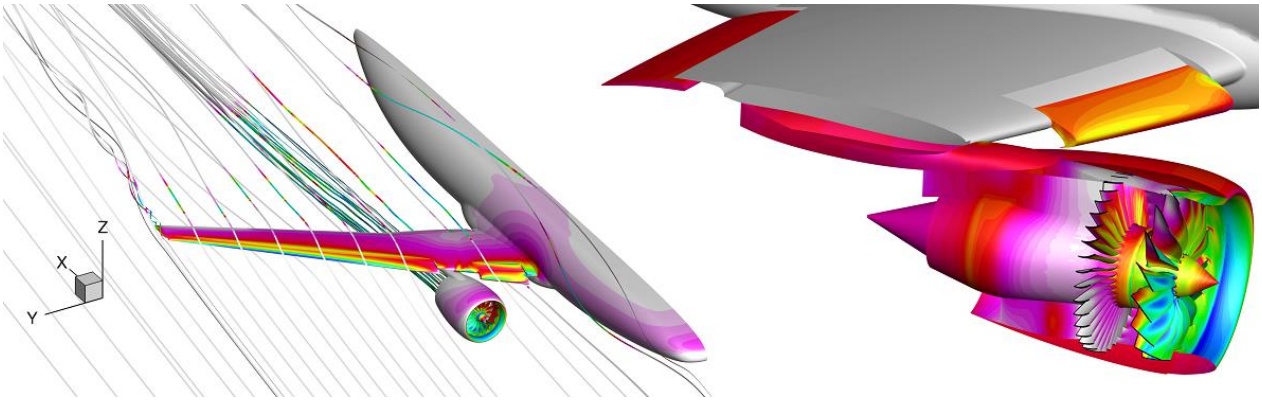

Figure 15: instantaneous result of a time-accurate simulation in take-off conditions with high-lift devices.

Figure 15 presents a visualisation of a time-accurate simulation, showing the wall pressure distribution both on the plane (left side of the figure) and inside the engine (right side). Ribbons coloured by turbulent viscosity allow to visualise the flow field both upstream (regular ribbons with low turbulence values) and in the wake of the airplane (ribbons following the velocity distribution and the vortex with high values of turbulence). When focussing on the right side of the image, the flow is similar to the one obtained in cruise conditions, presented in figure 4, besides the high-lift devices.

The simulations are ongoing and an analysis of the engine performance will be presented in a future work.

DOI: 10.13009/EUCASS2023-597

6 Conclusions

This article presented a summary of the activities performed by ONERA on the NOVASPIRE configuration in the frame of the European Clean Sky 2 programme (Large Passenger Aircraft platform). The configuration, representative of a civil aircraft equipped with an engine under the wing, is modelled in details, with a complete representation of some key elements as the rotating fan, the OGV and the high-lift devices when considering take-off conditions. After a brief presentation of the configuration and the activities linked to the grid preparation, the article presented the work necessary to prepare the simulation, which is particularly complex due to the Chimera assembly and the interfaces between fixed and rotating parts as well as the quantities investigated for analysing the performances.

The different approaches adopted have then been presented, illustrating the advantages of the steady-state simulations, which can yield satisfying results despite the spatial averaging needed for the mixing planes. Time-accurate simulations have then been illustrated, discussing the differences between the instantaneous results and the time-averaged ones. Both external and internal flow fields have been discussed, focusing on the stations following the definitions of the ASPIRE engine proposed by Airbus.

The performances of the engine have then been evaluated, by analysing both the mass-flow rates at different locations and the 0D parameters as pressure or temperature ratios and isentropic efficiencies. Grid convergence, turbulence-modelling and numerical scheme dependency has been briefly presented.

Overall, despite some difficulties linked to the complexity of the case, the work performed demonstrated the feasibility of such simulations, allowing for a full description of the complete configuration, without having to adopt any simplification of the geometry or the specifications of the engine. This work yielded a validation of the approach proposed by ONERA and demonstrated that RANS and URANS simulation are a valuable solution for analysing the installation effect when considering modern aircraft configuration equipped with UHBR engines, where the interaction between the airframe, the intake and the internal part of the engine are so important that more classical approach are no longer accurate.

Acknowledgements

This article presented a summary of the technical activities performed by ONERA on the NOVASPIRE aircraft concept in the framework of the European Clean Sky 2 programme, Large Passenger Platform (WP 1.1.13.1). The project has received funding from the Clean Sky 2 Joint Undertaking under the European Union's Horizon 2020 research and innovation program under grant agreement N°CS2-LPA-GAM-2022-2023. The author thanks the many colleagues involved in the study for their technical and scientific support as well as the Airbus partners for the involvement in the project.

References

[1] Peters, A., Spakovszky, Z. S., Lord, W. K., and Rose, B., “Ultrashort Nacelles for Low Fan Pressure Ratio Propulsors,” *Journal of Turbomachinery*, Vol. 137, No. 2, Sept. 2014

[2] L. Wiart, O. Atinault, B. Paluch, D. Hue, R. Grenon. “Development of NOVA Aircraft Configurations for Large Engine Integration Studies”, *AIAA 2015-225*.

[3] A. Burlot, F. Sartor, M. Vergez, M. Méheut, R. Barrier. “Method comparison for fan performance in short intake nacelle”, *AIAA 2018-4204*.

[4] M. Méheut, F. Sartor, M. Vergez, M. Laban, R. Schnell, A. Stuermer, G. Lefevre. “Assessment of Fan/Airframe aerodynamic performance using 360° uRANS computations: Code-to-Code comparison between ONERA, DLR, NLR and Airbus”, *AIAA 2019-0582*.

[5] Benoit, B., Péron, S., and Landier, S., “Cassiopee: A CFD pre- and post-processing tool,” *Aerospace Science and Technology*, Vol. 45, 2015, pp. 272-283.

[6] L. Cambier, S. Heib and S. Plot, "The Onera elsA CFD software: input from research and feedback from industry," *Mechanics and Industry*, vol. 14, pp. 159-174, 2013

[7] F. Sartor, A. Burlot and M. Méheut, “Numerical Simulations of Fan/Airframe Interaction with and without Active Flow-Control”, *AIAA 2018-3065*.